The Astrophysical Journal, 984:140 (11pp), 2025 May 10 https://doi.org/10.3847/1538-4357/adc1bf


# The Morphology and Kinematics of a Giant, Symmetric Nebula around a Radio-loud Quasar 3C 57: Extended Rotating Gas or Biconical Outflows?

Zhuoqi (Will) Liu[1], Sean D. Johnson[1], Jennifer I-Hsiu Li[2,3,4], Benoît Epinat[5,6], Gwen C. Rudie[7], Ana Monreal-Ibero[8], Sebastiano Cantalupo[9], Zhijie Qu[10], Mandy C. Chen[7,11], Wolfram Kollatschny[12], Sowgat Muzahid[13], Fakhri S. Zahedy[7,14], Elise Kesler[1], and Nishant Mishra[1]
[1] Department of Astronomy, University of Michigan, 1085 S. University, Ann Arbor, MI 48109, USA; zql@umich.edu
[2] Center for AstroPhysical Surveys, National Center for Supercomputing Applications, University of Illinois Urbana-Champaign, Urbana, IL 61801, USA
[3] Michigan Institute for Data Science, University of Michigan, Ann Arbor, MI 48109, USA
[4] Department of Astronomy, University of Michigan, Ann Arbor, MI 48109, USA
[5] Aix-Marseille Univ, CNRS, CNES, LAM (Laboratoire d'Astrophysique de Marseille), Marseille, France
[6] Canada-France-Hawaii Telescope, 65-1238 Mamalahoa Highway, Kamuela, HI 96743, USA
[7] The Observatories of the Carnegie Institution for Science, 813 Santa Barbara Street, Pasadena, CA 91101, USA
[8] Leiden Observatory, Leiden University, PO Box 9513, 2300 RA Leiden, The Netherlands
[9] Department of Physics, University of Milan Bicocca, Piazza della Scienza 3, I-20126 Milano, Italy
[10] Department of Astronomy & Astrophysics, The University of Chicago, 5640 S. Ellis Avenue, Chicago, IL 60637, USA
[11] Cahill Center for Astronomy and Astrophysics, California Institute of Technology, Pasadena, CA 91125, USA
[12] Institut für Astrophysik und Geophysik, Universität Göttingen, Friedrich-Hund Platz 1, D-37077 Göttingen, Germany
[13] Inter-University Centre for Astronomy and Astrophysics (IUCAA), Post Bag 4, Ganeshkhind, Pune 411 007, India
[14] Department of Physics, University of North Texas, Denton, TX 76201, USA
*Received 2025 January 8; revised 2025 March 6; accepted 2025 March 16; published 2025 May 6*

## Abstract

Gas flows between galaxies and the circumgalactic medium play a crucial role in galaxy evolution. When ionized by a quasar, these gas flows can be directly traced as giant nebulae. We present a study of a giant nebula around a radio-loud quasar, 3C 57 at $z \approx 0.672$. Observations from MUSE reveal that the nebula is elongated with a major axis of 70 kpc and a minor axis of 40 kpc. The nebula displays an approximately symmetric blueshifted–redshifted pattern along the major axis and multicomponent emission features in its [O II] and [O III] profiles. The morphology and kinematics can be explained as rotating gas or biconical outflow, both of which qualitatively reproduce the observed position–velocity diagram. The 3C 57 nebula is significantly more kinematically disturbed, with $W_{80}$ (the line width encompassing 80% of the flux) of approximately 300–400 km s$^{-1}$, compared to H I gas in local early-type galaxies, which typically shows $W_{80} \approx 50$ km s$^{-1}$. This velocity dispersion is comparable to the gas in cool-core clusters despite originating in a group 100 times less massive. For biconical outflow models, the inferred 10°–20° inclination angle is in tension with the unobscured nature of the quasar, as the dusty torus is expected to be perpendicular to the outflow. Neither a quiescent rotating gas origin nor an biconical outflow fully reproduces the observed kinematics and morphology of the 3C 57 nebula, suggesting a more intricate origin likely involving both rotation and active galactic nuclei feedback.

*Unified Astronomy Thesaurus concepts:* Circumgalactic medium (1879); Cool intergalactic medium (303); Quasars (1319)

## 1. Introduction

The baryon cycle, encompassing both gas inflows and outflows between galaxies and the circumgalactic medium (CGM)/intergalactic medium (IGM), is central to understanding galaxy evolution. Inflows supply galaxies with fresh material, driving star formation and black hole growth (e.g., C. Chiappini et al. 1997; L. J. Tacconi et al. 2013), while outflows, driven by processes such as active galactic nuclei (AGN) and stellar outflows (for a review, see A. C. Fabian 2012; D. Zhang 2018), tidal interactions (e.g., A. Marasco et al. 2016), and ram pressure stripping (e.g., J. A. Hester 2006), return enriched gas to the CGM/IGM. These feedback mechanisms also expel heavy elements produced by stars and supernovae from the interstellar matter (ISM) into the CGM/IGM to reproduce the observed mass–metallicity relation (e.g., C. A. Tremonti et al. 2004; X. Ma et al. 2016). Consequently, studying the gas exchange around galaxies offers valuable insights into the processes shaping galaxy formation and evolution, and it is ranked as a key, long-term priority by the 2020 Decadal Survey (National Academies of Sciences 2021).

Large-scale gas reservoirs can be directly observed through H I 21 cm emission in the local Universe. However, observations of 21 cm emission from diffuse gas reservoirs are not currently possible beyond the local Universe. Most CGM observations in the distant Universe therefore rely on sensitive absorption spectroscopy of UV-bright background sources passing through the halos of foreground galaxies (for a review, see J. Tumlinson et al. 2017). This approach, however, has inherent limitations in constraining the morphology and spatially resolved kinematics of gas flows except in rare cases (H.-W. Chen et al. 2014; S. Lopez et al. 2018). Alternatively, gas flows around galaxies, along with their morphology and kinematics, can be directly traced by observations of giant nebulae using cutting-edge wide-field integral field spectrographs (IFS) such as the Multi-Unit Spectroscopic Explorer (MUSE; R. Bacon et al. 2010). Deep, coadded MUSE

observations enable the detection of CGM emission around galaxies in Ly$\alpha$, [O II], Mg II, and Si II (e.g., L. Wisotzki et al. 2016; R. Dutta et al. 2023; Y. Guo et al. 2023, 2024; H. Kusakabe et al. 2024, H. Zhang & D. Zaritsky 2024). However, such observations typically require tens to hundreds of hours of integration time to achieve the necessary sensitivity, making them resource intensive.

Systems such as quasars substantially elevate the local ionizing radiation background, which increases the ionization rate and consequently the recombination rate under photoionization equilibrium. This also boosts the hydrogen ionization fraction and the number of metal ions such as $O^+$ and $O^{2+}$ in the surrounding IGM/CGM, leading to an amplified emission in recombination and collisionally excited lines. At $z > 2$, systematic IFS surveys revealed ubiquitous giant H I Ly$\alpha$ nebulae around radio-quiet quasars extending over 100 kpc (e.g., S. Cantalupo et al. 2014; E. Borisova et al. 2016; Z. Cai et al. 2019; D. B. O'Sullivan et al. 2020; M. Fossati et al. 2021; R. Mackenzie et al. 2021). At $z < 1.5$, the capabilities of IFS have led to discoveries of giant nebulae around quasars emitting in [O II], H$\beta$, and [O III] (e.g., S. D. Johnson et al. 2018, 2022, 2024; J. M. Helton et al. 2021; Z. Liu et al. 2024).

The Cosmic Ultraviolet Baryon Surveys (CUBS; H.-W. Chen et al. 2020) and the MUSE Quasar Blind Emitters Survey (MUSEQuBES; e.g., S. Dutta et al. 2024) were designed to study CGM and IGM surrounding galaxies at $z \approx 0.1$–1.4, leveraging high-quality Cosmic Origins Spectrograph absorption spectra of UV luminous quasars. Such investigations necessitate comprehensive galaxy redshift surveys, achievable with deep MUSE observations. As a result, CUBS and MUSEQuBES acquired 30 deep MUSE data cubes around UV luminous, unobscured quasars at $z = 0.4$–1.4. These data serendipitously enable observations of rest-optical emission around the quasars. S. D. Johnson et al. (2024) recently reported the frequent detection of large ionized circumgalactic nebulae around UV luminous quasars in these fields. Some of the nebulae exhibit irregular or filamentary morphologies, consistent with interactions and accretion, while others exhibit more regular morphologies. Comprehensive studies exploring the nebulae with irregular and filamentary morphologies have been published (e.g., S. D. Johnson et al. 2018, 2022; J. M. Helton et al. 2021; Z. Liu et al. 2024), but no case studies have yet focused on nebulae with regular morphologies and kinematics. In this paper, we present the first case study of a nebula with a regular morphology and kinematics resembling those of rotation or biconical outflows around a radio-loud quasar at $z < 1$, 3C 57 in the CUBS +MUSEQuBES survey.

Throughout the paper, we adopt a flat $\Lambda$ cosmology with $\Omega_m = 0.3$, $\Omega_\Lambda = 0.7$, and $H_0 = 70\,\mathrm{km\,s^{-1}\,Mpc^{-1}}$. All magnitudes are given in the AB system (J. B. Oke & J. E. Gunn 1983), unless otherwise stated. We use proper kiloparsecs as the unit of distance.

## 2. Observations and Data

The quasar 3C 57 hosts a ≈70 kpc scale circumgalactic nebula, discovered as one of larger nebulae around 30 UV luminous quasars at $z < 1$ (S. D. Johnson et al. 2024). To investigate this nebula, we observed the quasar field around 3C 57 using MUSE on the Very Large Telescope as part of MUSEQuBES survey (PI: J. Schaye, PID: 094.A-0131(B) and 096.A-0222(A)). We obtained four exposures collected between 2015 August 23rd and 2015 October 11th with a total exposure time of 2.0 hr with median seeing full-width-at-half-maximum (FWHM) conditions of 0.″7. We then reduced the MUSE data using three independent pipelines: CubEx (S. Cantalupo et al. 2019), the MUSE Guaranteed Time Observations (GTO) team pipeline (P. M. Weilbacher et al. 2014), and the ESO reduction pipeline (P. M. Weilbacher et al. 2012). All three pipelines produced consistent results, although with some differences in illumination corrections and night-sky-subtraction (for more details, see E. K. Lofthouse et al. 2020; S. D. Johnson et al. 2024). For simplicity, we converted the air wavelengths provided by the three pipelines to vacuum wavelengths.

To study faint extended emission, we performed quasar light subtraction to remove both continuum and line emission from the spatially unresolved narrow-line and broad-line regions in the nucleus, following the method described in S. D. Johnson et al. (2018) and J. M. Helton et al. (2021). This technique leverages the differences in spectral energy distribution between quasars and galaxies instead of relying on point-spread function measurements. Previous applications have demonstrated its effectiveness in eliminating spatially unresolved continuum, broad-line emissions, and narrow-line emissions from the nucleus.

We also obtained an image from the Advanced Camera for Surveys (ACS) on the Hubble Space Telescope (HST) to enable a more sensitive and higher angular resolution characterization of galaxies in the quasar field. The image was taken in the F814W filter (PI: L. Straka, PID: 14660) with an exposure time of 2179 s. We obtained the reduced image from the Barbara A. Mikulski Archive for Space Telescopes (MAST). To ensure uniformity in astrometry, we aligned the MUSE data cube and HST image with Gaia astrometry system using `Astrometry v1.5` (L. Wenzl 2022).

## 3. Results

### 3.1. Quasar Properties

3C 57 is a luminous, radio-loud quasar (M. P. Véron-Cetty & P. Véron 2006). To estimate its redshift, luminosity, and black hole mass, we extracted the MUSE spectrum with `MPDAF` (R. Bacon et al. 2016) before performing quasar and continuum subtraction. We chose an extraction aperture of $r = 3''$, and measured the systemic redshift of the quasar by fitting the [O II] $\lambda\lambda$3727, 3729 doublet with a Gaussian profile. Following P. C. Hewett & V. Wild (2010), we assumed a centroid of $\lambda$3728.6 for the doublet, expected from a 0.8 to 0.9: 1 doublet ratio. We found $z = 0.6718 \pm 0.0002$, where the uncertainty reflects the scatter between the [O II] centroid and stellar absorption lines of SDSS quasars at a similar redshift (P. C. Hewett & V. Wild 2010).

In addition, we fit the extracted quasar's spectrum with the Python QSO fitting code (`PyQSOFit`; H. Guo et al. 2019) to estimate the bolometric luminosity and the black hole mass of 3C 57. `PyQSOFit` models a quasar's spectrum with a combination of a power-law continuum, Fe II template, and sets of Gaussian line profiles for both the broad- and narrow-lines. From the fit, we computed a monochromatic luminosity at 5100 Å of $\lambda L_{5100} \approx 6.9 \times 10^{45}\,\mathrm{erg\,s^{-1}}$ and a bolometric luminosity of $L_{\mathrm{bol}} \approx 6.3 \times 10^{46}\,\mathrm{erg\,s^{-1}}$ using the bolometric correction factor from G. T. Richards et al. (2006). Finally, we determined an FWHM of H$\beta$ as $3900\,\mathrm{km\,s^{-1}}$ and used the

corresponding single-epoch virial theorem relations from M. Vestergaard & B. M. Peterson (2006) to infer a black hole mass of $M_{\rm BH} \approx 10^{8.9} M_{\odot}$. According to J. Kormendy & L. C. Ho (2013), this black hole mass corresponds to a stellar mass of $M_{*} \approx 10^{11.2} M_{\odot}$ for the host galaxy, although this stellar mass may have a >0.5 dex uncertainty due to the systematic uncertainty in single-epoch black hole mass estimates and the scatter in the black hole mass–stellar mass relations.

### 3.2. The Group Environment of 3C 57

Radio-loud quasars typically reside in overdense environments with a halo mass of $\approx 10^{13} M_{\odot}$, as determined from clustering studies (Y. Shen et al. 2009). Interactions between galaxies can strip gas from a galaxy's ISM/CGM, and lead to the formation of giant quasar nebulae when this gas falls within the quasar's ionization cone (S. D. Johnson et al. 2018; Z. Liu et al. 2024). Therefore, characterizing the group environment of the quasar is crucial before investigating the properties of the nebula.

To study the galactic environment of 3C 57, we conducted a galaxy survey on 3C 57, as detailed in J. M. Helton et al. (2021) and Z. Liu et al. (2024). In brief, we started by identifying continuum objects in both MUSE white light and the ACS+F814W images. We then fit each identified object with a linear combination of SDSS galaxy eigenspectra (A. S. Bolton et al. 2012) to obtain the galaxy redshift. We computed the best-fit linear combination on a grid ranging from $z = 0$ to $z = 1$ with a step size of $\Delta z = 0.0001$, recording the goodness-of-fit statistic ($\chi^2$) over the entire grid. We adopted the redshift with the minimum global $\chi^2$ as our initial solution and then visually inspected each best-fit model to ensure robustness. For galaxies with both emission and absorption lines, we masked out strong emission lines and measured the redshift based on stellar absorption features when possible. This approach helps avoid potential bias in redshift measurements from large-scale nebulae in the field that may not be closely associated with the galaxies in question. From previous applications, the typical uncertainty in redshift measurements is $\sigma \approx 20\,{\rm km\,s^{-1}}$ (J. M. Helton et al. 2021).

In the MUSE field of 3C 57, we identified six galaxies including the quasar host, with line-of-sight (LOS) velocities $|\Delta v| < 1500\,{\rm km\,s^{-1}}$ of the quasar systemic velocity. Outside MUSE field of view (FoV), ongoing wide-field spectroscopy follow-up with Magellan does not identify any potential group members within 500 kpc from the quasar. Four of the six associated galaxies are more than 75 kpc away from the quasar, and three of them are actively star forming. One galaxy, G2, is near the quasar centroid, and its redshift can only be measured from emission lines. Additionally, we detected a galaxy G1 (not included as one of the six galaxies), which might be at the quasar's systemic redshift. However, its redshift cannot be determined due to its proximity to the quasar. Compared to other quasars with similar UV luminosity and MUSE survey depth, the number of group members around 3C 57 is slightly below average, but remains within the expected range for radio-loud systems, which typically host 3–23 galaxies (J. I. H. Li et al. 2024), although this estimate is derived from a limited sample.

For the six group galaxies, we computed a mean LOS velocity of $\Delta v_{\rm group} = 100\,{\rm km\,s^{-1}}$ relative to the quasar's systemic velocity. Due to the fact that the sample standard deviation estimator is statistically biased in the small $N_{\rm gal}$ regime, we calculated a bias-corrected velocity dispersion of $\sigma_{\rm group} = 200\,{\rm km\,s^{-1}}$ following A. Ferragamo et al. (2020). We then estimated a halo mass of $\log(M_{\rm halo}/M_{\odot}) \approx 12.7$ using Equation (1) from E. Munari et al. (2013). In contrast, UV luminous quasars with more than five group members typically inhabit halos with masses of $\log(M_{\rm halo}/M_{\odot}) \approx 13.5 \pm 0.6$, and radio-loud quasars are generally found in even larger halos, with masses of $\log(M_{\rm halo}/M_{\odot}) \approx 13.5-14.6$ (J. I. H. Li et al. 2024). This suggests that 3C 57 resides in a less massive halo compared to typical UV luminous quasar systems.

### 3.3. Giant Nebula Characteristics

Ionizing radiation from the accretion disks of AGN can ionize the gas to large distances, causing it to emit in recombination and collisionally excited lines such as [O II], H$\beta$, and [O III]. As a result, wide-field IFS observations of quasar fields often reveal large nebulae. In this paper, we adopted the same methodology as S. D. Johnson et al. (2024), who presented the discovery of 3C 57 nebula after conducting quasar light subtraction, continuum subtraction, and optimal extraction. We performed continuum subtraction locally for the [O II] and [O III] emission lines around the quasar, as described in Z. Liu et al. (2024). We first fit the continuum to the blue and red sides of these lines after masking the spectral region within $\pm$500–1000 km s$^{-1}$ of the expected observed wavelength at the quasar's redshift. We then conducted optimal extraction with 3D segmentation, as described in S. D. Johnson et al. (2024).

This 3D segmentation technique is widely applied in the detection of giant Ly$\alpha$ nebulae at higher redshift (E. Borisova et al. 2016; F. Arrigoni Battaia et al. 2019; K. N. Sanderson et al. 2021). In summary, we first smoothed the data cube in both the spatial and spectral dimensions with a $\sigma = 1.5$ pixel Gaussian kernel, and created a signal-to-noise ratio (S/N) data cube. For each wavelength slice, we identified spaxels with a threshold of S/N > 1.5 in the smoothed S/N data cube, connected adjacent spaxels above this threshold, and required at least 10 connected spaxels to define a detection. We began with the detection having the largest connected area, which defined its spatial segmentation. We then identified the wavelength slice where this largest connected area is. For spectral segmentation, we started at this layer and identified the continuous wavelength range (in both increasing and decreasing directions) meeting the threshold for each spaxel in the spatial segmentation, stopping when the condition was no longer met. We repeated this process for the detection with the second largest area after masking the previous detection, continuing until no additional detections remained. We then integrated the unsmoothed flux in each spaxel over the spectral interval defined by the 3D segmentation to create surface brightness maps. For pixels falling below the S/N threshold, we used a background level of three spectral pixels at the wavelength where the mean S/N per pixel of the nebula is highest. The resulting [O II] and [O III] surface brightness maps for 3C 57 are shown in Figure 1, revealing a giant $\approx$70 kpc nebula.

To quantify the kinematics of the nebula, we jointly fit Gaussian line profiles to the quasar and continuum subtracted [O II] and [O III] data cubes. To enhance S/N, we first smoothed the data with a $\sigma = 0\farcs3$ Gaussian kernel, which we choose to match the seeing disk. We incorporated the segmentation map from the optimal extraction to define the

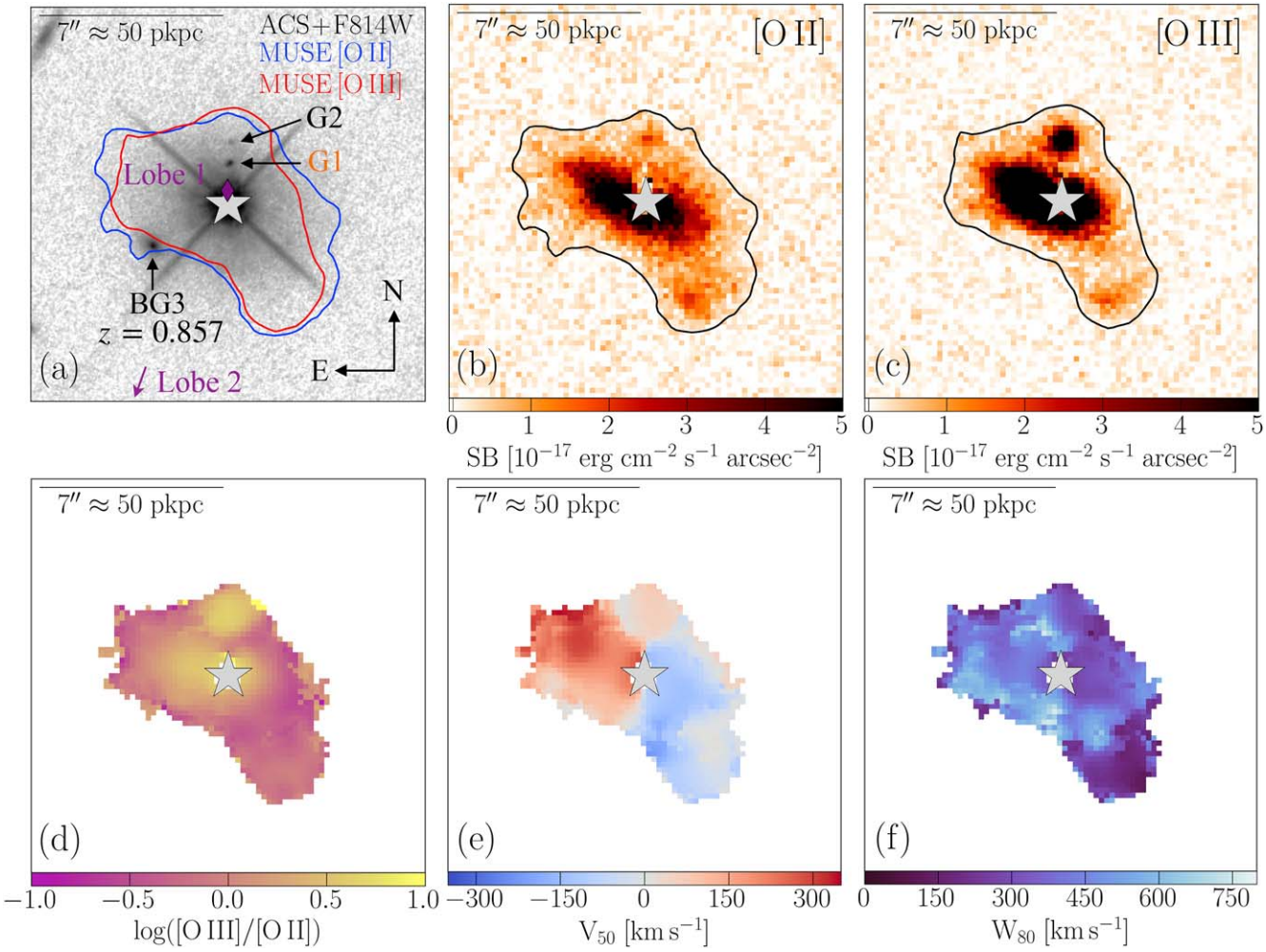


**Figure 1.** Visualizations of the nebula around 3C 57. Panel (a): HST ACS+F814W image of the field, with galaxies labeled with their IDs. The centroid of one radio lobe is marked with a purple diamond, while the second radio lobe lies outside the FoV and is indicated with a purple arrow. Panel (b) and panel (c): narrowband [O II] and [O III] surface brightness maps generated from optimal extraction. These maps are overlaid with [O II] and [O III] surface brightness contours at levels of $0.2 \times 10^{-17}$erg cm$^{-2}$ s$^{-1}$ arcsec$^{-2}$. The contours shown in panel (b) and panel (c) are overlaid on the HST image in blue and red, respectively. Panel (d): map of nebular photoionization shown as the line ratio [O III]$\lambda$5008/[O II]$\lambda\lambda$3727 + 3729. Panel (e) and panel (f): maps of the nebular $V_{50}$ and $W_{80}$.

spatial fitting region. We initially fit a single kinematic component to the [O II] and [O III] emission lines in every spaxel of the nebula. Specifically, we jointly fit two Gaussian profiles for the [O II] doublet and one Gaussian profile for [O III], with shared redshift and velocity dispersion parameters across all lines. In most cases, the kinematic parameters shared by [O II] and [O III] result in good fits to the data, but in spaxels where the line profiles of [O II] and [O III] are inconsistent, we add an additional component to [O III] with significant flux, while this component contributes negligible flux in [O II]. We then adjusted the number of components based on the fit quality, evaluating both $\chi^2$ and the Bayesian Information Criterion (BIC). If adding more components led to a lower BIC, we adopted the solution with the higher number of components (for more information on this approach, see A. R. Liddle 2007). For the majority of the spaxels in the nebula, one or two Gaussians are adequate to describe the line profile, although three components are needed in some regions. We note that complex kinematic features are easier to detect for spaxels with higher S/N. Therefore, we are more likely to miss line asymmetry at the edge of the nebula due to lower S/N. Finally, we visually inspected all spaxels to check if the best-fit model sufficiently reproduces the data. To visualize the kinematics of the nebula and compare with the literature (e.g., G. Liu et al. 2013a), we produced $V_{50}$ and $W_{80}$ maps, which visualize the line center and width. In brief, we measured velocities at which a fraction of the model line flux is accumulated. $V_{50}$ corresponds to the velocity at 50% of the cumulative flux of the fitted Gaussian models. $W_{80}$ represents the line width between the velocity range at 10% and 90% of the cumulative flux. We used the [O III] line profiles to construct these maps whenever it is possible, and used [O II] when [O III] is not detected. For most spaxels with detections of both lines, [O II] and [O III] yield consistent $V_{50}$ and $W_{80}$ measurements. The resulting $V_{50}$, and $W_{80}$ maps are displayed in panels (e) and (f) of Figure 1, respectively.

To study the ionization state of the nebula, we also produced a [O III]/[O II] line ratio map by taking the ratio of the integrated fluxes of these lines. For spaxels not detected in [O III], we computed $3\sigma$ upper limits using [O III] error arrays by summing over the spectral dimension within a range determined by the [O II] optimal extraction. This map provides an opportunity to study the spatial dependence and distribution of the kinematics and the ionization state of the gas. The [O III]/[O II] (O32) line ratio map is shown in panel (d). To further characterize the ionization state, we computed the

geometric median, defined as the median value across all spaxels, and found log[O32] $\approx -0.05$. Since this value is dominated by less luminous regions and is not representative of the entire nebula, we also estimated a cumulative O32 by dividing the total [O III] flux by the total [O II] flux across the entire nebula, yielding log[O32] $\approx 0.20$. These values are higher than those of typical massive star-forming galaxies (median log[O32] $\approx -0.40$; M. Paalvast et al. 2018).

To investigate the ionization source of the nebula, we estimated an approximate log([O III]/H$\beta$) $\approx 0.7$. This suggests the nebula is ionization bounded (large optical depth), as a matter-bounded cloud would exhibit a significantly lower log([O III]/H$\beta$) due to oxygen being ionized beyond the $O^{2+}$ state, while H$\beta$, as a recombination line, remains unaffected (G. Liu et al. 2013b; Z. Liu et al. 2024). Additionally, we found higher ionization state lines, including [Ne III]$\lambda$3869 and [Ne V]$\lambda$3427 in the inner region of the nebula. The ionization potential for $Ne^{4+}$ is 97 eV (B. T. Draine 2011), far exceeding the 54 eV required to produce $He^{2+}$, the highest energy photons typically generated in large numbers by stellar populations. Moreover, quasars with similar UV luminosity have been observed to ionize nebulae over large distances, as seen in Z. Liu et al. (2024). These factors support photoionization by the quasar (e.g., B. A. Groves et al. 2004), essentially ruling out star formation as the primary ionization source for most of the nebula. However, the observed line ratios could also be explained by fast shocks, as the nebular kinematics align with the velocities required to produce them (Z. Liu et al. 2024). Thus, the ionization mechanism remains ambiguous, with both quasar photoionization and fast shocks as viable explanations. To determine if dust affects these line ratios, we estimate the Balmer-line ratios at $\approx$4 kpc (0.″5) east of the quasar centroid, where the surface brightness is the highest. With an extraction radius of $\approx$7 kpc (1″), we find H$\gamma$/H$\beta$ $\approx 0.48 \pm 0.08$, consistent with Case B recombination (D. E. Osterbrock & G. J. Ferland 2006) in the absence of dust.

To examine the nebula and any relationship with galaxies in the quasar environment, we overlaid [O II] and [O III] emission contours over the HST image in panel (a) of Figure 1. We detected three galaxies enclosed or partly enclosed by the nebula. Galaxy G1 is spatially aligned with the northern part of the nebula, but its redshift remains undetermined due to insufficient S/N after quasar light subtraction. G2 corresponds to the bright knot in [O III], indicating its spatial coincidence with the nebula. BG3 on the southeast side is a background galaxy at a redshift of $z \approx 0.857$ determined from stellar absorption lines detected in the MUSE spectrum and therefore unassociated with the nebula. Overall, the majority of the nebula does not closely align with nearby galaxies, suggesting that it is not arising from ongoing galaxy interactions.

The radio-loud quasar 3C 57 exhibits two prominent radio lobes (R. Morganti et al. 1993; R. I. Reid et al. 1999). One lobe is centered near the quasar, while the other is located 15″ southeast, corresponding to 100 kpc at the quasar's redshift. To illustrate their positions relative to the quasar, we overlay the VLASS radio lobe positions on the HST image in panel (a) of Figure 1 (M. Lacy et al. 2020). The central lobe is marked with a purple diamond, while the southeastern lobe, located outside the FoV, is indicated by a purple arrow. The 3C 57 nebula does not extend to the southeast radio lobe, but spatially overlaps with and surrounds the other radio lobe near the quasar's centroid, in the last projection.

The giant nebula surrounds the quasar with projected radii of $d \approx 10$–30 kpc, and exhibits LOS velocities of $V_{50} \approx -250$ to $+250$ km s$^{-1}$. Notably, the nebula displays a fairly symmetric blueshifted–redshifted pattern from the northeast to the southwest along the major axis. This kind of symmetric blueshifted–redshifted pattern can be produced by approximately edge-on rotation or biconical outflows. However, these two scenarios would produce distinct velocity dispersion maps. Gas in rotating disks typically show more quiescent kinematics with $\sigma \approx 25$–100 km s$^{-1}$, or equivalently $W_{80} \approx 60$–250 km s$^{-1}$ (see discussion), while gas disturbed by outflows typical have $W_{80} > 400$ km s$^{-1}$ (B. Husemann et al. 2016). The $W_{80}$ map of 3C 57 aligns more with the characteristics expected from outflows, showing velocity dispersions ranging from $W_{80} \approx 300$ to 700 km s$^{-1}$, with peaks in several spots over the northern and southern extensions. An exception is the southwestern edge of the nebula, which exhibits quiescent kinematics. This region is kinematically distinct, with a $W_{80}$ of 150 km s$^{-1}$, significantly lower than the rest of the nebula.

To better explore the complex kinematics of the nebula, we show a [O II] line profile map in Figure 2. We first stacked the $\lambda$3727 and $\lambda$3729 components of each kinematic component, and then summed all components in each spaxel to create the final map. Each cell corresponds to a spaxel in the MUSE data cube, and it is colored by the respective $V_{50}$ value. This map allows us to visualize how line profiles correspond to the $V_{50}$ in each spaxel and observe changes in the detailed line profile at different regions of the nebula. In particular, the nebula exhibits multicomponent emission features on both the blueshifted and redshifted sides, with a stronger presence on the redshifted side. In most spaxels with multicomponent profiles, the individual components are blended, with centroid separations smaller than their respective widths, except in a few spaxels above the quasar centroid, likely due to residuals from quasar light subtraction. Additionally, the northern knot of the nebula around G2 exhibits complex kinematics with a broad wing and a narrow core that we interpreted as the emission from the galaxy G2. In conclusion, the nebula displays complex emission features with broad emission wings.

## 4. Discussion

The discovery of a giant nebula requires both the presence of gas and its positioning within quasar's ionization cone. Gas arising from filamentary inflows, stellar and AGN feedback, galaxy interactions, and ISM/CGM gas of the host galaxy can create galactic-scale structures with regions ionized by the quasar. This gas will emit in recombination and collisionally excited lines, producing giant quasar nebulae. Depending on the gas origin, quasar nebulae might exhibit distinct morphology, kinematics, and galactic environment. Specifically, the majority of the nebula around 3C 57 is not morphologically or kinematically related to galaxies in the quasar host group, suggesting that it does not originate from interactions. Moreover, the nebula does not exhibit long filaments, which are expected from inflows. Instead, the nebula exhibits a blueshifted–redshifted pattern along the major axis, which can be produced by biconical outflows with proper alignment. The nebula also shows multicomponent emission features with large dispersion. Such features are commonly observed around luminous quasars due to AGN feedback (e.g., J. E. Greene et al. 2012; G. Liu et al. 2013b). These features suggest that the 3C 57 nebula may originate from AGN

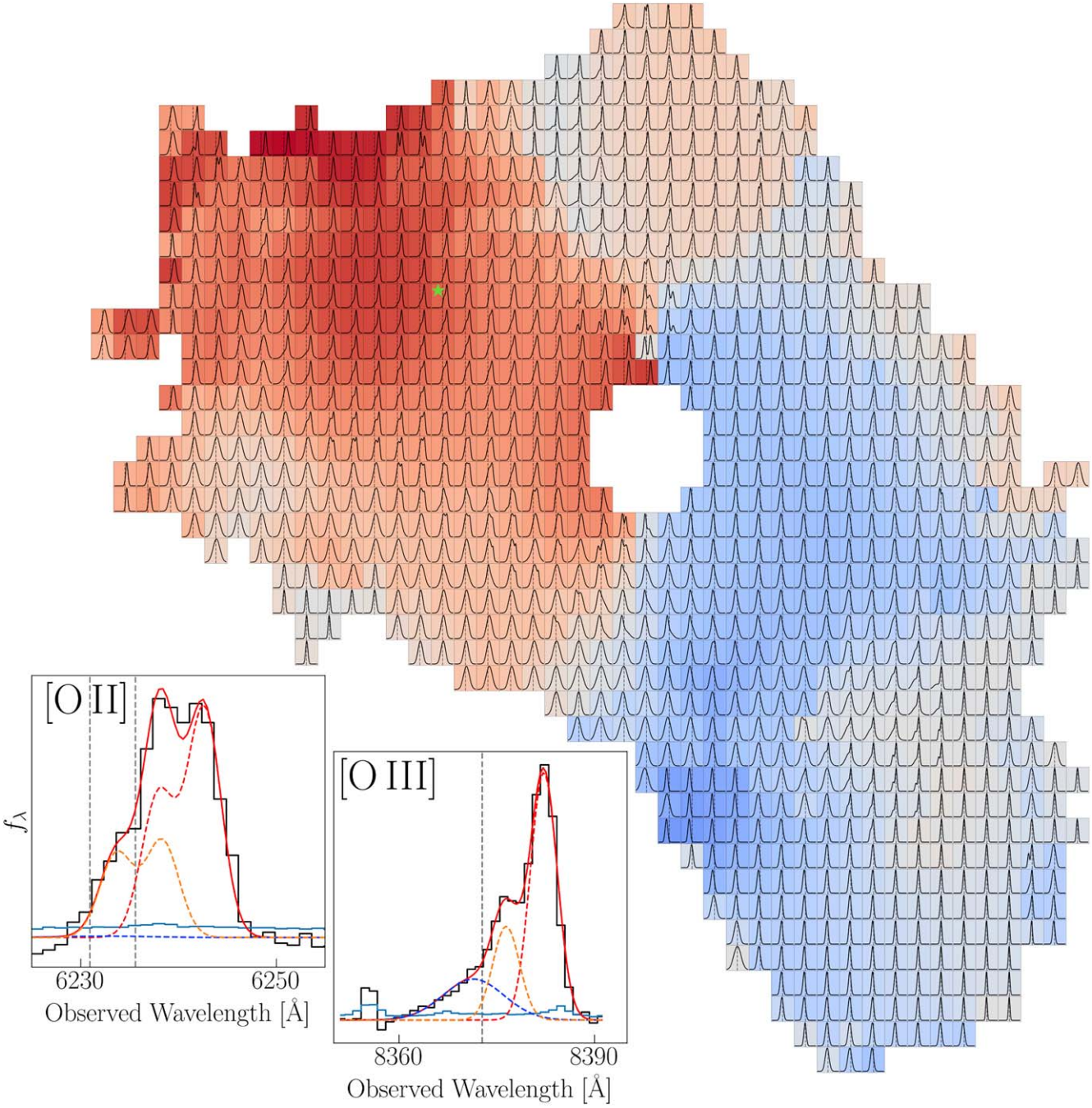


**Figure 2.** [O II] line profiles of the 3C 57 nebula, with each cell corresponding to a spaxel in the MUSE data cube. Cells are colored based on their $V_{50}$ values, and the fitted [O II] line profiles are shown in black, with a vertical line marking the quasar's systemic velocity. Profiles are normalized to unity, and each panel spans a velocity range of $\pm 800$ km s$^{-1}$. This map was generated by first stacking the $\lambda$3727 and $\lambda$3729 components of each profile, and then show the summation of all profiles as a function of velocity. Two examples of line fitting for [O II] and [O III] in a spaxel are shown in the bottom left, with its position on the nebula marked as a green star. The extracted spectrum and error array are shown as solid black and blue lines, respectively. The best-fit models are shown as dashed red, orange, and blue lines, respectively, for each profile. For reference, 20 Å in [O II] and 30 Å in [O III], respectively, corresponds to 1000 km s$^{-1}$. Multicomponent emission features are seen across both the blueshifted and redshifted sides of the nebula, with a more prominent presence on the redshifted side. In most spaxels with multicomponent profiles, the individual components are blended, with centroid separations smaller than their respective widths, except in a few spaxels above the quasar centroid, likely due to residuals from quasar light subtraction.

feedback. However, extended rotating gas can also produce a similar blueshifted–redshifted pattern. Such extended rotating gas around massive ellipticals can originate from extended ISM/CGM disks that are kinematically aligned with the stellar component, or from late-stage mergers resulting in misalignment of the stellar and gas kinematics (P. Serra et al. 2012). In some cases, 21 cm emission around elliptical galaxies exhibits rotation-like kinematics but with circular velocity less than expected for such massive systems, suggesting the presence of net inflows or motion along elliptical orbits (F. Fraternali et al. 2001). In these cases, the gas may have become part of the host galaxy and settled into regular rotation around the stellar body over several Gyr. We will explore these possibilities in Sections 4.1 and 4.2.

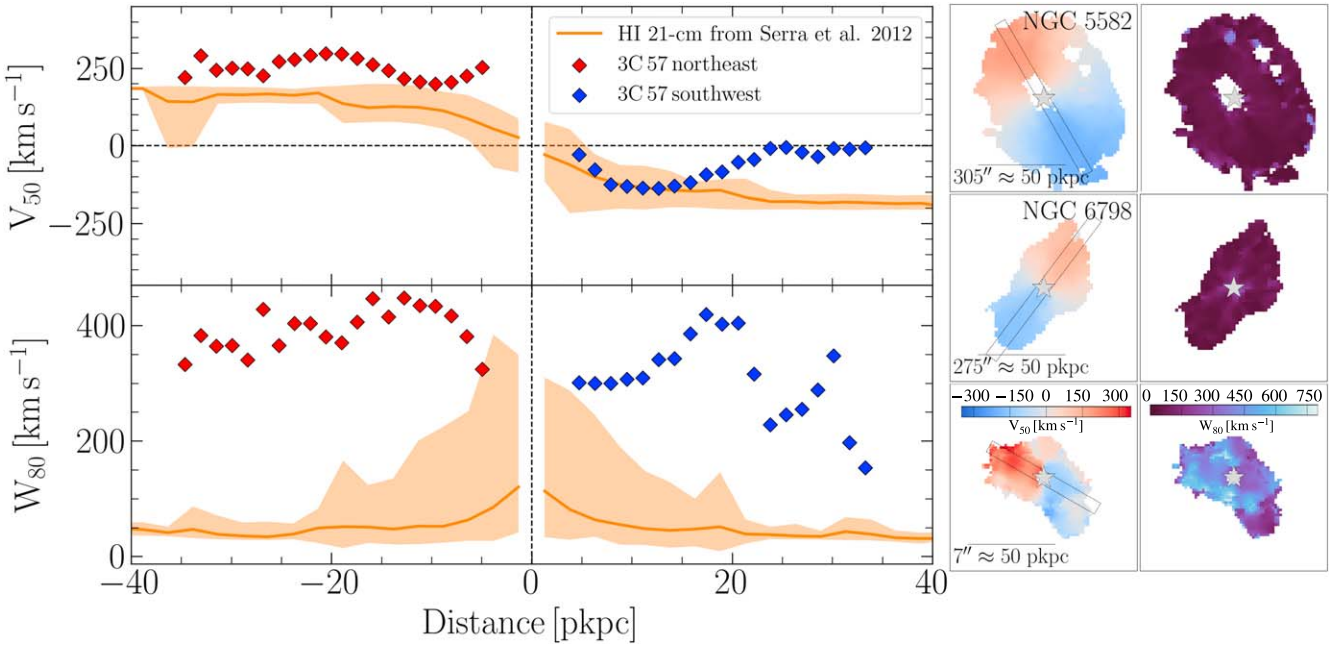


**Figure 3.** Left: Position–velocity and –velocity dispersion diagrams of 3C 57 and H I gas in early-type galaxies (P. Serra et al. 2012). The radial profiles of $V_{50}$ and $W_{80}$ are shown, respectively, in the top and bottom panel. The binned 3C 57 profiles are shown as red and blue diamonds representing northeast and southwest portion of the nebula. The mean radial profile of early-type galaxies is shown as a solid line, and the filled orange region marks the minimum and maximum value in each bin. Right: $V_{50}$ and $W_{80}$ maps of NGC 6798, NGC 5582, and 3C 57 with the same colormaps shown in Figure 1. The dashed rectangles in the left column represent the extraction slits with a width of 7 kpc, used to obtain the radial profiles shown on the left. 3C 57 resembles early-type galaxies in its $V_{50}$ map and profile, while the $W_{80}$ shows significant discrepancies, suggesting the nebula around 3C 57 is not typical extended rotating gas from a galaxy.

### *4.1. Extended Rotating Gas*

One possibility is that the nebula primarily consists of rotating ISM and CGM gas from the quasar's host galaxy. If such gas is ionized by the quasar, it could produce a blueshifted–redshifted pattern along the major axis. To explore this, we compared the nebula's morphology and kinematics with H I gas detected around local early-type galaxies through 21 cm emission. H I 21 cm serves as an appropriate analog for the gas detected in optical emission around 3C 57, which may have been neutral in the absence of ionizing photons from the luminous quasar.

We used data from the ATLAS$^{3D}$ H I survey, which contains 21 cm observations of 166 early-type galaxies in the local Universe (M. Cappellari et al. 2011; P. Serra et al. 2012). From this sample, we selected galaxies classified as having large H I disks/rings by P. Serra et al. (2012), characterized by regular rotation and a distribution extending beyond the galaxy's stellar body. We further refined our selection to include galaxies with gas disks comparable in size (40–100 kpc) to the nebula around 3C 57, excluding those with clear spiral structures. Our final set of galaxies includes NGC 2685, NGC 3941, NGC 3945, NGC 4262, NGC 5582, NGC 6798, and UGC 06176 (R. Morganti et al. 2006; G. I. G. Józsa et al. 2009; T. Oosterloo et al. 2010; P. Serra et al. 2012, 2014). The stellar masses of these galaxies range from $\log(M_*/M_\odot) \approx 10.3$ to $\approx 11.0$, derived from detailed axisymmetric dynamical modeling (M. Cappellari et al. 2013). To produce the $V_{50}$ and $W_{80}$ maps, we measured the velocity dispersion of H I in these galaxies by fitting the data cube with a single Gaussian, using the ATLAS$^{3D}$ H I velocity maps as initial guesses. We then extracted kinematic profiles of the $V_{50}$ and $W_{80}$ maps using a pseudoslit placed along the major axis, with a fixed width of 7 kpc and length of 100 kpc. To facilitate a comparison, we stacked the radial profiles of all galaxies and computed a mean profile, bounded by the minimum and maximum values. Figure 3 displays this stacked profile alongside example $V_{50}$ and $W_{80}$ maps, in comparison to 3C 57.

H I gas in early-type galaxies exhibits some similarities in amplitude and pattern in $V_{50}$ maps and profiles to the 3C 57 nebula (see Figure 3), although there are notable differences. An asymmetry is observed between the blueshifted and redshifted sides, with the blueshifted side approaching zero velocity starting at 15 kpc, while the redshifted side reaches an amplitude of 250 km s$^{-1}$. This asymmetry arises from the presence of a luminous redward component on the blueshifted side and an extremely redward component on the redshifted side, which shift the velocities toward their corresponding values. The maximum velocity of the redshifted side is $\approx +250$ km s$^{-1}$ while that of the blueshifted side is $\approx -150$ km s$^{-1}$, representing a nonnegligible asymmetry that exceeds the expected uncertainty in the quasar systemic redshift. Additionally, they differ significantly in velocity dispersion. The H I gas typically has a $W_{80} \approx 50$ km s$^{-1}$, in contrast to the nebula's $W_{80} \approx 300$–$400$ km s$^{-1}$. We note that the kinematically quiescent region near the southwestern edge of the nebula exhibits $W_{80} \approx 150$ km s$^{-1}$, which is lower than the rest of the nebula and causes the $W_{80}$ to plateau at +30 kpc, but it is still elevated compared to the H I gas detected in 21 cm around elliptical galaxies. Moreover, the extended H I gas generally lacks multicomponent emission, unlike 3C 57. The kinematic inconsistencies between the nebula and the H I gas suggest that the 3C 57 nebula might not consist solely of rotating ISM/CGM gas from the host galaxy. Instead, the gas may be related to rotation, but also disturbed by another process such as AGN feedback.

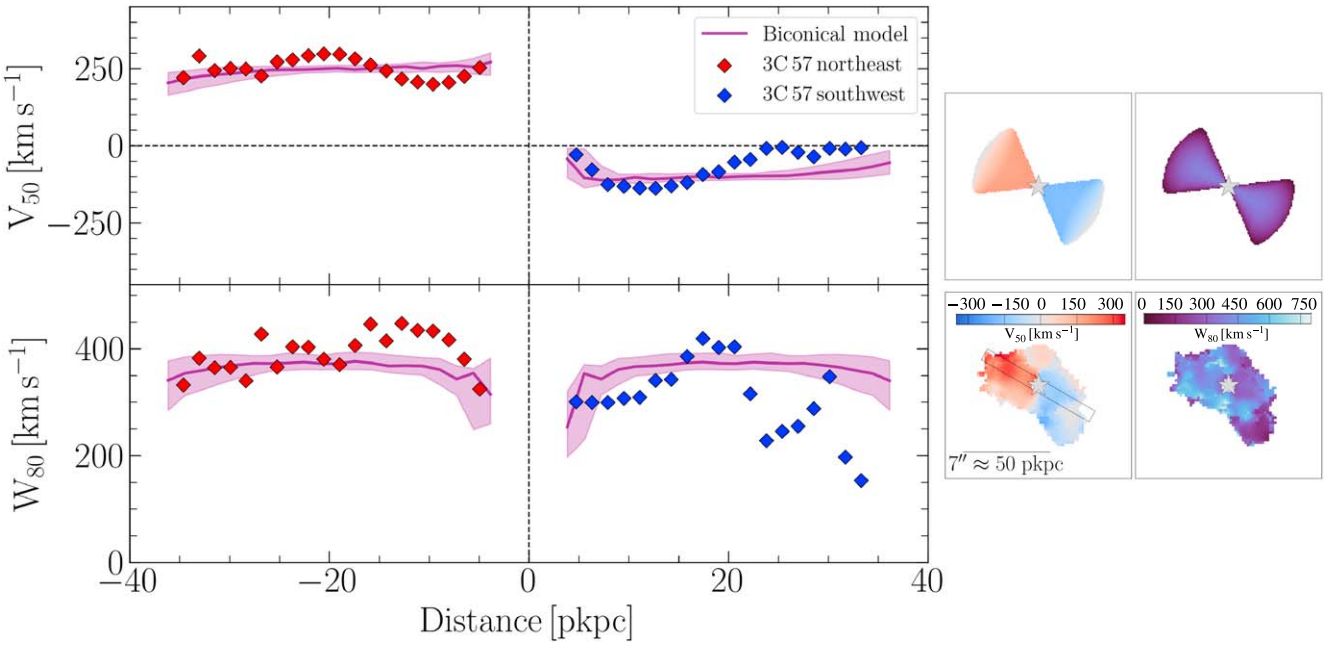


**Figure 4.** Same as Figure 3 but for biconical models. The median posterior radial profile of the biconical models is shown as solid lines, and the filled purple region marks the minimum and maximum value in each bin. Right: $V_{50}$ and $W_{80}$ maps of the best-fit biconical model. Biconical outflow models can qualitatively reproduce the observed position–velocity and –velocity dispersion diagrams. However, the inferred 10°–20° inclination angle conflicts with the unobscured nature of the quasar, as the dusty torus is expected to be perpendicular to the outflow. Additionally, the nebula exhibits notably stronger emission along the minor axis compared to the model predication, underscoring the limitations of simple geometric models in fully capturing the complex nature of quasar nebulae.

### 4.2. AGN Feedback

AGN feedback presents another plausible explanation for the nebula's origin. In this scenario, outflowing gas powered by the AGN extends from the nucleus, often forming a biconical structure. Biconical outflows are commonly observed in local Seyfert galaxies and have been extensively modeled to study the kinematics of the narrow line region (NLR) in both Seyferts (e.g., D. M. Crenshaw & S. B. Kraemer 2000a; S. Veilleux et al. 2001) and quasars (e.g., H.-Y. Shih & A. Stockton 2014), and may be responsible for extended, asymmetric line emission detected along the minor axis in stacks around massive, early-type galaxies (H. Zhang & D. Zaritsky 2022). Moreover, these models effectively reproduce various observed phenomena, including position–velocity diagrams (D. M. Crenshaw & S. B. Kraemer 2000b) and line profiles (H.-J. Bae & J.-H. Woo 2016; C. Marconcini et al. 2023). When inclined to the LOS, biconical outflows can produce a symmetric blueshifted–redshifted pattern, multicomponent emission features, and large velocity dispersion. These characteristics align well with our observations of the 3C 57 nebula, making the AGN feedback scenario a strong contender for explaining its origin and properties.

To determine whether a biconical model can reproduce the kinematics, we generated models following H.-J. Bae & J.-H. Woo (2016) and C. Marconcini et al. (2023) and performed Markov Chain Monte Carlo (MCMC) analysis. Each model is parameterized by three rotation angles, a velocity profile, semi-inner and semiouter opening angles ($\theta_{\rm in}$, $\theta_{\rm out}$), and a flux profile. Due to the bicone's axial symmetry and the ability to rotate the model based on 3C 57's position angle, we reduced three rotation angles to a single inclination angle. The inclination is defined such that an edge-on bicone corresponds to zero inclination, while a face-on scenario results in a single visible cone projected as a circular region. To create the relatively flat $V_{50}$ and $W_{80}$ profile, we adopted a constant velocity profile and a slow-decaying flux profile $f(r) = f_0\, e^{-\frac{r}{r_0}}$, where $f_0$ is the apex flux, and $r_0$ is a variable scale-radius. Based on experimentation, we assume a non-hollow geometry ($\theta_{\rm in} = 0$), as the observed line profile and position–velocity profile are inconsistent with hollow models. Our final model is characterized by three parameters: inclination angle ($\beta$), constant outflow velocity ($v_{\rm out}$), and semiouter opening angle ($\theta_{\rm out}$).

We generated models within parameter grids of $5° < \beta < 50°$, $350\,{\rm km\,s^{-1}} < v_{\rm out} < 1500\,{\rm km\,s^{-1}}$, and $10° < \theta_{\rm out} < 50°$, following the ranges used in H.-J. Bae & J.-H. Woo (2016), but extend to greater values to accommodate potential model variations. We then extracted and interpolated the velocity and velocity dispersion profiles along the bicone's major axis using `RegularGridInterpolator` function from `scipy`. Additionally, we introduced a free parameter to allow for the velocity shift between the outflow and the measured quasar redshift. Finally, we ran MCMC with `emcee` (D. Foreman-Mackey et al. 2013) to estimate posteriors given the observed $V_{50}$ and $W_{80}$ profiles. During the minimization process, we imposed a velocity error floor of $20\,{\rm km\,s^{-1}}$ to account for systematic errors from the kinematics fitting.

The biconical outflow models can qualitatively reproduce the observed kinematics, and the resulting posteriors indicate a range of viable configurations. The parameter ranges that yield likely models are $13° < \beta < 22°$, $350\,{\rm km\,s^{-1}} < v_{\rm max} < 720\,{\rm km\,s^{-1}}$, and $21° < \theta_{\rm out} < 43°$. Among these, the best-fit model has parameters of $\beta = 20°$, $v_{\rm max} = 460\,{\rm km\,s^{-1}}$, and $\theta_{\rm out} = 34°$. Figure 4 displays the PV diagrams from these posteriors, with the best-fit model shown as a purple line and the region between minimum and maximum values from all posteriors shaded. While the biconical models capture the overall kinematics, they fail to quantitatively reproduce certain

features, such as the gradual $V_{50}$ drop and $W_{80}$ fluctuation at 20 kpc on the blueshifted side.

### 4.3. An Ambiguous Origin

Both extended rotating gas and biconical outflow models can qualitatively reproduce the blueshifted–redshifted pattern and velocity profile observed in the 3C 57 nebula. However, unlike the 3C 57 nebula, the H I gas in the extended rotating gas scenario exhibits quiescent kinematics and does not display an elevated velocity dispersion. While biconical models can qualitatively reproduce the observed velocity and velocity dispersion values, the small inclination angle derived from fitting the biconical outflow model is in tension with the unobscured nature of the quasar. Biconical outflows are more often observed in obscured AGN (H. R. Schmitt & A. L. Kinney 1996), which is expected from the unified model for AGN, where the dusty torus is perpendicular to the outflowing cones (e.g., C. M. Urry & P. Padovani 1995). Therefore, with an inclination of 10°–20°, we would expect an obscured quasar, which is inconsistent with the observed characteristics of 3C 57. Additionally, we expect the line profiles from a biconical outflow to exhibit symmetry between the blueshifted and redshifted sides. In particular, the models predict that emission profiles on the blueshifted side will exhibit a lower surface brightness redward wing, and a similar blueward wing on the redshift side. However, the data reveal luminous blueshifted wings across nearly the entire nebula (see Figure 2). Moreover, the strong emission along the minor axis is not reproduced by the biconical models. These discrepancies highlight the limitations of simple geometric models in fully capturing the complex nature of quasar nebulae. Together, these findings suggest that neither model alone can fully explain the observed phenomena, indicating a more intricate interplay between the nebula's kinematics and its underlying processes.

Alternatively, the 3C 57 nebula may originate from a combination of rotating gas and AGN feedback. In this scenario, the blueshifted–redshifted pattern could result from the rotating gas of the quasar's host galaxy, while the multicomponent emission features with elevated dispersion may be induced by feedback processes. Similarly, elevated dispersion in molecular gas can be found in poststarburst galaxies, where strong turbulence is seen along with regularly rotating systems (e.g., A. Smercina et al. 2022; K. D. French et al. 2023). This scenario implies a dynamic interplay between the host galaxy's ISM/CGM and the AGN's energetic output. Such a model would explain the coexistence of the blueshifted–redshifted pattern and elevated dispersion, as well as the difficulty in fitting the data to simpler, single-origin models.

### 4.4. Comparisons with Other Nebulae

While both rotating gas and biconical outflow models cannot fully reproduce all observed features, we expanded our analysis by comparing the 3C 57 nebula with other nebulae around UV luminous quasars reported in the CUBS+MUSE-QuBES survey. Within this survey, 3C 57 stands out as one of the nebulae with the highest velocity dispersions, alongside TXS 0206 − 048 and J 2135 − 5316. TXS 0206 − 048 showcases $W_{80} \approx 450\,\mathrm{km\,s^{-1}}$, possibly related to strong turbulence (M. C. Chen et al. 2024), while J 2135 − 5316 has $W_{80} \approx 425\,\mathrm{km\,s^{-1}}$ and exhibits complex multicomponent emission features, possibly due to AGN feedback. In comparison, nebulae arising from interactions generally have lower dispersions, with $\sigma \approx 60$–$130\,\mathrm{km\,s^{-1}}$ ($W_{80} \approx 150$–$325\,\mathrm{km\,s^{-1}}$) (see Figure 8 of M. C. Chen et al. 2024; also see S. D. Johnson et al. 2018, 2022; J. M. Helton et al. 2021; Z. Liu et al. 2024). None of the reported nebulae with elevated dispersion exhibit the distinct blueshifted–redshifted pattern seen in 3C 57. In future work, we will provide a comprehensive characterization of giant nebulae in the CUBS+MUSEQuBES survey, with the potential to identify more samples of nebulae exhibiting blueshifted–redshifted features and gain deeper insights into their origins.

Additionally, the brightest cluster galaxies (BCGs) in cool-core clusters are useful analogs for understanding the origin of the 3C 57 nebula. In these clusters, cool gas around BCGs is heated by energetic AGN feedback, with observable radio jets and X-ray cavities. [O II] nebulae near the positions of radio lobes and X-ray cavities have a velocity dispersion of $\sigma > 200\,\mathrm{km\,s^{-1}}$, or equivalently $W_{80} > 500\,\mathrm{km\,s^{-1}}$ (M.-J. Gingras et al. 2024). Additionally, elevated dispersions are observed in regions away from cavities, often in a direction roughly perpendicular to them in cool-core clusters. These features may indicate strong bipolar outflows, potentially from jets that either are unseen or have changed orientation over time (M.-J. Gingras et al. 2024). In the case of 3C 57, two radio lobes are present: one centered near the quasar and another located 15″ southeast (see Figure 1). The 3C 57 nebula does not extend to the southeast radio lobe, but is overlapped with the other radio lobe near the quasar's centroid. One possibility is that this central radio lobe indicates the presence of a jet impacting the nearby CGM and ISM, potentially accounting for the elevated dispersion observed in the nebula. Alternatively, the lobe may result from strong nuclear radio emission rather than a jet, with feedback that either are undetected or have shifted orientation over time. Regardless, 3C 57 could serve as an intriguing low-mass analog to cool-core clusters, providing a unique perspective on how AGN-driven feedback and outflows might operate in lower-mass environments.

## 5. Summary and Conclusions

In this paper, we presented a case study of a giant nebula around a radio-loud quasar at $z \approx 0.672$ based on MUSE observations of the field of 3C 57. We found that the giant, ≈70 kpc scale nebula around 3C 57 exhibits a blueshifted–redshifted pattern with large velocity dispersion and multi-component emission features. The observed active kinematics and blueshifted–redshifted morphology suggest that the nebula is unlikely to be solely rotating ISM/CGM gas from the host galaxy. Instead, the nebula's characteristics indicate a more complex origin, potentially resulting from a combination of rotating gas and AGN feedback mechanisms.

While the 3C 57 nebula provides a unique case study of the intricate interplay between AGN activity and host galaxy kinematics, our work will expand to analyze other nebulae in the CUBS+MUSEQuBES survey to determine if any exhibit a similar blueshifted–redshifted pattern. Insights from the 3C 57 nebula may also shed light to the studies of other giant nebulae around starburst galaxies and galaxy groups (e.g., B. Epinat et al. 2018; A. Boselli et al. 2019; H.-W. Chen et al. 2019; D. S. N. Rupke et al. 2019; J. N. Burchett et al. 2021; J. Zabl et al. 2021; F. Leclercq et al. 2022; R. Dutta et al. 2023; B. Epinat et al. 2024). Future IFSs, such as LLAMAS

(G. Furesz et al. 2020), IFUM (M. Mateo et al. 2022), Blue MUSE (J. Richard 2019), and MIRMOS (N. P. Konidaris et al. 2020), will further drive discoveries of giant nebulae, and uncover more systems like 3C 57 to offer deeper insights.

## Acknowledgments

We thank the anonymous referee for the constructive and insightful comments, which significantly improved this paper. We thank Z.L.'s thesis committee members, Camille Avestruz, Eric Bell, Joel Bregman, and Feige Wang, for their valuable comments and discussions. S.D.J. and Z.L. acknowledge partial support from HST-GO- 15280.009-A, HST-GO-15298.007-A, HST-GO-15655.018-A, and HST-GO-15935.021-A. S.C. gratefully acknowledges support from the European Research Council (ERC) under the European Union's Horizon 2020 Research and Innovation program grant agreement No. 864361. J.I.L. is supported by the Eric and Wendy Schmidt AI in Science Postdoctoral Fellowship, a Schmidt Futures program. M.C.C. is supported by the Brinson Foundation through the Brinson Prize Fellowship Program. This paper is based on observations from the European Organization for Astronomical Research in the Southern Hemisphere under ESO (PI: J. Schaye, PID: 094.A-0131(B) and 096.A-0222(A)), and the NASA/ESA Hubble Space Telescope (PI: L. Straka, PID: 14660). The reduced HST image can be found in MAST: doi:10.17909/x948-mv36. Additionally, this paper made use of the NASA/IPAC Extragalactic Database, the NASA Astrophysics Data System, `Astropy` (Astropy Collaboration et al. 2022), `Aplpy` (T. Robitaille & E. Bressert 2012), and `Photutils` (L. Bradley 2023).

## Data Availability

The data used in this paper are available from the ESO and HST data archives.

## ORCID iDs

Zhuoqi (Will) Liu https://orcid.org/0000-0002-2662-9363
Sean D. Johnson https://orcid.org/0000-0001-9487-8583
Jennifer I-Hsiu Li https://orcid.org/0000-0002-0311-2812
Benoît Epinat https://orcid.org/0000-0002-2470-5756
Gwen C. Rudie https://orcid.org/0000-0002-8459-5413
Ana Monreal-Ibero https://orcid.org/0000-0002-6455-2491
Sebastiano Cantalupo https://orcid.org/0000-0001-5804-1428
Zhijie Qu https://orcid.org/0000-0002-2941-646X
Mandy C. Chen https://orcid.org/0000-0002-8739-3163
Wolfram Kollatschny https://orcid.org/0000-0002-0417-1494
Sowgat Muzahid https://orcid.org/0000-0003-3938-8762
Fakhri S. Zahedy https://orcid.org/0000-0001-7869-2551
Elise Kesler https://orcid.org/0000-0001-6846-9399
Nishant Mishra https://orcid.org/0000-0002-9141-9792

## References

Arrigoni Battaia, F., Obreja, A., Prochaska, J. X., et al. 2019, A&A, 631, A18
Astropy Collaboration, Price-Whelan, A. M., Lim, P. L., et al. 2022, ApJ, 935, 167
Bacon, R., Accardo, M., Adjali, L., et al. 2010, Proc. SPIE, 7735, 773508
Bacon, R., Piqueras, L., Conseil, S., Richard, J., & Shepherd, M. 2016, MPDAF: MUSE Python Data Analysis Framework, Astrophysics Source Code Library, ascl:1611.003
Bae, H.-J., & Woo, J.-H. 2016, ApJ, 828, 97
Bolton, A. S., Schlegel, D. J., Aubourg, É., et al. 2012, AJ, 144, 144
Borisova, E., Cantalupo, S., Lilly, S. J., et al. 2016, ApJ, 831, 39
Boselli, A., Epinat, B., Contini, T., et al. 2019, A&A, 631, A114
Bradley, L. 2023, astropy/photutils: v1.8.0, Zenodo, doi:10.5281/zenodo.7946442
Burchett, J. N., Rubin, K. H. R., Prochaska, J. X., et al. 2021, ApJ, 909, 151
Cai, Z., Cantalupo, S., Prochaska, J. X., et al. 2019, ApJS, 245, 23
Cantalupo, S., Arrigoni-Battaia, F., Prochaska, J. X., Hennawi, J. F., & Madau, P. 2014, Natur, 506, 63
Cantalupo, S., Pezzulli, G., Lilly, S. J., et al. 2019, MNRAS, 483, 5188
Cappellari, M., Emsellem, E., Krajnović, D., et al. 2011, MNRAS, 413, 813
Cappellari, M., Scott, N., Alatalo, K., et al. 2013, MNRAS, 432, 1709
Chen, H.-W., Boettcher, E., Johnson, S. D., et al. 2019, ApJL, 878, L33
Chen, H.-W., Gauthier, J.-R., Sharon, K., et al. 2014, MNRAS, 438, 1435
Chen, H.-W., Zahedy, F. S., Boettcher, E., et al. 2020, MNRAS, 497, 498
Chen, M. C., Chen, H.-W., Rauch, M., et al. 2024, ApJ, 962, 98
Chiappini, C., Matteucci, F., & Gratton, R. 1997, ApJ, 477, 765
Crenshaw, D. M., & Kraemer, S. B. 2000a, ApJ, 532, 247
Crenshaw, D. M., & Kraemer, S. B. 2000b, ApJL, 532, L101
Draine, B. T. 2011, Physics of the Interstellar and Intergalactic Medium (Princeton, NJ: Princeton Univ. Press)
Dutta, R., Fossati, M., Fumagalli, M., et al. 2023, MNRAS, 522, 535
Dutta, S., Muzahid, S., Schaye, J., et al. 2024, MNRAS, 528, 3745
Epinat, B., Contini, T., Finley, H., et al. 2018, A&A, 609, A40
Epinat, B., Contini, T., Mercier, W., et al. 2024, A&A, 683, A205
Fabian, A. C. 2012, ARA&A, 50, 455
Ferragamo, A., Rubiño-Martìn, J. A., Betancort-Rijo, J., et al. 2020, A&A, 641, A41
Foreman-Mackey, D., Hogg, D. W., Lang, D., & Goodman, J. 2013, PASP, 125, 306
Fossati, M., Fumagalli, M., Lofthouse, E. K., et al. 2021, MNRAS, 503, 3044
Fraternali, F., Oosterloo, T., Sancisi, R., & van Moorsel, G. 2001, ApJL, 562, L47
French, K. D., Smercina, A., Rowlands, K., et al. 2023, ApJ, 942, 25
Furesz, G., Simcoe, R. A., Egan, M., et al. 2020, Proc. SPIE, 11447, 114470A
Gingras, M.-J., Coil, A. L., McNamara, B. R., et al. 2024, ApJ, 977, 159
Greene, J. E., Zakamska, N. L., & Smith, P. S. 2012, ApJ, 746, 86
Groves, B. A., Dopita, M. A., & Sutherland, R. S. 2004, ApJS, 153, 9
Guo, H., Liu, X., Shen, Y., et al. 2019, MNRAS, 482, 3288
Guo, Y., Bacon, R., Bouché, N. F., et al. 2023, Natur, 624, 53
Guo, Y., Bacon, R., Wisotzki, L., et al. 2024, A&A, 688, A37
Helton, J. M., Johnson, S. D., Greene, J. E., & Chen, H.-W. 2021, MNRAS, 505, 5497
Hester, J. A. 2006, ApJ, 647, 910
Hewett, P. C., & Wild, V. 2010, MNRAS, 405, 2302
Husemann, B., Scharwächter, J., Bennert, V. N., et al. 2016, A&A, 594, A44
Johnson, S. D., Chen, H.-W., Straka, L. A., et al. 2018, ApJL, 869, L1
Johnson, S. D., Liu, Z. W., Li, J. I. H., et al. 2024, ApJ, 966, 218
Johnson, S. D., Schaye, J., Walth, G. L., et al. 2022, ApJL, 940, L40
Józsa, G. I. G., Oosterloo, T. A., Morganti, R., Klein, U., & Erben, T. 2009, A&A, 494, 489
Konidaris, N. P., Rudie, G. C., Newman, A. B., et al. 2020, Proc. SPIE, 11447, 114471E
Kormendy, J., & Ho, L. C. 2013, ARA&A, 51, 511
Kusakabe, H., Mauerhofer, V., Verhamme, A., et al. 2024, A&A, 691, A255
Lacy, M., Baum, S. A., Chandler, C. J., et al. 2020, PASP, 132, 035001
Leclercq, F., Verhamme, A., Epinat, B., et al. 2022, A&A, 663, A11
Li, J. I. H., Johnson, S. D., Boettcher, E., et al. 2024, ApJ, 965, 143
Liddle, A. R. 2007, MNRAS, 377, L74
Liu, G., Zakamska, N. L., Greene, J. E., Nesvadba, N. P. H., & Liu, X. 2013a, MNRAS, 436, 2576
Liu, G., Zakamska, N. L., Greene, J. E., Nesvadba, N. P. H., & Liu, X. 2013b, MNRAS, 430, 2327
Liu, Z., Johnson, S. D., Li, J. I. H., et al. 2024, MNRAS, 527, 5429
Lofthouse, E. K., Fumagalli, M., Fossati, M., et al. 2020, MNRAS, 491, 2057
Lopez, S., Tejos, N., Ledoux, C., et al. 2018, Natur, 554, 493
Ma, X., Hopkins, P. F., Faucher-Giguère, C.-A., et al. 2016, MNRAS, 456, 2140
Mackenzie, R., Pezzulli, G., Cantalupo, S., et al. 2021, MNRAS, 502, 494
Marasco, A., Crain, R. A., Schaye, J., et al. 2016, MNRAS, 461, 2630
Marconcini, C., Marconi, A., Cresci, G., et al. 2023, A&A, 677, A58
Mateo, M., Bailey, J. I., Song, Y., et al. 2022, Proc. SPIE, 12184, 121845P
Morganti, R., de Zeeuw, P. T., Oosterloo, T. A., et al. 2006, MNRAS, 371, 157
Morganti, R., Killeen, N. E. B., & Tadhunter, C. N. 1993, MNRAS, 263, 1023
Munari, E., Biviano, A., Borgani, S., Murante, G., & Fabjan, D. 2013, MNRAS, 430, 2638
National Academies of Sciences 2021, Pathways to Discovery in Astronomy and Astrophysics for the 2020s (Washington, DC: The National Academies Press)
Oke, J. B., & Gunn, J. E. 1983, ApJ, 266, 713

Oosterloo, T., Morganti, R., Crocker, A., et al. 2010, MNRAS, 409, 500
Osterbrock, D. E., & Ferland, G. J. 2006, Astrophysics of Gaseous Nebulae and Active Galactic Nuclei (Sausalito, CA: Univ. Science Books)
O'Sullivan, D. B., Martin, C., Matuszewski, M., et al. 2020, ApJ, 894, 3
Paalvast, M., Verhamme, A., Straka, L. A., et al. 2018, A&A, 618, A40
Reid, R. I., Kronberg, P. P., & Perley, R. A. 1999, ApJS, 124, 285
Richard, J. 2019, in The Very Large Telescope in 2030 (Garching: ESO), 24
Richards, G. T., Lacy, M., Storrie-Lombardi, L. J., et al. 2006, ApJS, 166, 470
Robitaille, T., & Bressert, E. 2012, APLpy: Astronomical Plotting Library in Python, Astrophysics Source Code Library, ascl:1208.017
Rupke, D. S. N., Coil, A., Geach, J. E., et al. 2019, Natur, 574, 643
Sanderson, K. N., Prescott, M. K. M., Christensen, L., Fynbo, J., & Møller, P. 2021, ApJ, 923, 252
Schmitt, H. R., & Kinney, A. L. 1996, ApJ, 463, 498
Serra, P., Oosterloo, T., Morganti, R., et al. 2012, MNRAS, 422, 1835
Serra, P., Oser, L., Krajnović, D., et al. 2014, MNRAS, 444, 3388
Shen, Y., Strauss, M. A., Ross, N. P., et al. 2009, ApJ, 697, 1656
Shih, H.-Y., & Stockton, A. 2014, ApJ, 786, 3
Smercina, A., Smith, J.-D. T., French, K. D., et al. 2022, ApJ, 929, 154
Tacconi, L. J., Neri, R., Genzel, R., et al. 2013, ApJ, 768, 74
Tremonti, C. A., Heckman, T. M., Kauffmann, G., et al. 2004, ApJ, 613, 898
Tumlinson, J., Peeples, M. S., & Werk, J. K. 2017, ARA&A, 55, 389
Urry, C. M., & Padovani, P. 1995, PASP, 107, 803
Veilleux, S., Shopbell, P. L., & Miller, S. T. 2001, AJ, 121, 198
Véron-Cetty, M. P., & Véron, P. 2006, A&A, 455, 773
Vestergaard, M., & Peterson, B. M. 2006, ApJ, 641, 689
Weilbacher, P. M., Streicher, O., Urrutia, T., et al. 2012, Proc. SPIE, 8451, 84510B
Weilbacher, P. M., Streicher, O., Urrutia, T., et al. 2014, in ASP Conf. Ser. 485, Astronomical Data Analysis Software and Systems XXIII, ed. N. Manset & P. Forshay (San Francisco, CA: ASP), 451
Wenzl, L. 2022, lukaswenzl/astrometry: Astrometry v1.5, Zenodo, doi:10.5281/zenodo.6462441
Wisotzki, L., Bacon, R., Blaizot, J., et al. 2016, A&A, 587, A98
Zabl, J., Bouché, N. F., Wisotzki, L., et al. 2021, MNRAS, 507, 4294
Zhang, D. 2018, Galax, 6, 114
Zhang, H., & Zaritsky, D. 2022, ApJ, 941, 18
Zhang, H., & Zaritsky, D. 2024, SciA, 10, eadp8629